Testing a Paul trap through determining the evaporation rate of levitated single semi-volatile organic droplets

A. VALENZUELA,[1,2,*] **R. A. RICA,**[1] **F. J. OLMO-REYES,**[1,2] **AND L. ALADOS-ARBOLEDAS**[1,2]

[1]*Department of Applied Physics, University of Granada, Granada 18071, Spain*
[2]*Andalusian Institute for Earth System Research (IISTA-CEAMA), Granada 18006, Spain*
*avalenzuela@ugr.es

Abstract: Rigorous knowledge of the optical fingerprint of droplets is imperative for the understanding of complex aerosol processes. Here, a Paul trap is operated to store single semi-volatile organic droplets in air. The droplets are illuminated with a green laser and the elastic scattering is collected on a CMOS camera. The setup provides excellent performance in terms of confinement and stability, allowing us to detect size changes of the order of few nanometres. The stability also allows us to measure vapour pressures with remarkable reproducibility. This approach supplies a robust method for the optical interrogation in the sub-micron range.

1. Introduction

The physical and chemical features of aerosols are essential signatures that must be understood and quantified for a broad range of purposes. From particles and clouds in the atmosphere, haze and fog, pollution, industrial processes, and the spreading of biological organisms and pathogens (pollen, bacteria, viruses, etc.), aerosols can be linked to respiratory, cardiovascular, infectious and allergic diseases [1–3].

The understanding of the process of droplet evaporation is a highly demanding task and considerable uncertainties still remain [4]. This knowledge is pivotal in numerous disciplines such as in the evolution of climate [5], transpiration in plants [6] or drug delivery [7–9]. The accomplishment of accurate analysis of the evaporation of droplets is challenging because it is notably laborious to determine vapour pressure of pure compounds in the liquid phase, as well as the activities of the components in the condensed phase occurring in the atmosphere [10]. Aerosol ensembles allow measurements of vapour pressures on supersaturated aqueous solutions. However, the required precision in measuring small size changes of droplets over time often prevent measurements that are sensible to fluctuations in atmospheric variables like temperature and relative humidity [11]. Indeed, ensemble aerosol techniques supply averaged values of physicochemical properties over large ranges of droplets sizes, shapes and compositions [12–14]. This averaging leads to measurements with inadequate accuracy for quantitatively evaluating aerosol processes. In order to avoid invasive aerosol manipulation, single droplet tools can yield new outlooks over the evaporation processes. In low and steady relative humidity (RH) (<10%) the droplet shrinking indicates the evaporation of semi-volatile compounds and can be exploited to estimate the vapour pressure. In this RH range, size changes need to be measured with a higher exactitude in comparison with other approaches; hence, single droplet techniques seem suited to evaluate the vapour pressure of semi-volatile droplets improving gas-droplet partitioning. Multiple publications about hygroscopicity and evaporation of single aerosol droplets using electrodynamic balances and optical trapping have been addressed [15–22]. Nevertheless, reported vapour pressures of semi-volatile individual aerosol compounds measured by different techniques still present large differences [23]. Indeed, [16] reported a vapour

pressure mean value of 7.5 ± 2.5 mPa for five glycerol individual droplets using optical trapping, whereas [11] provided a mean value of 15.1 mPa with errors of +1.1 mPa and -0.5 mPa with a similar levitation scheme. Therefore, the high variability of pure component vapour pressures values reported in the literature for organic compounds, with low vapour pressures, limits the improvement of laboratory techniques and the model validations.

Single droplet levitation tools have contributed with an extraordinary perspective to assess individual optical and thermodynamic processes avoiding inconsistency coming up from the complexity of the aerosol in the atmosphere. However, these methodologies have been used for analysing specific droplet size ranges. For instance, the electrodynamic balance apparatus has offered highly accurate measurements of droplet hygroscopicity, but has been largely focused in studying droplets larger than 4-10 µm in diameter [24,25]. Individual atmospheric droplets with diameters below 1 µm in size have been barely studied using these laboratory techniques. However, they have an exceptional significance from the point of view of their atmospheric implications [26,27]. A huge step forward, within fine mode range, was performed in Ref. [28], where an accurate parameterization of real refractive index, as function of wavelength and relative humidity, for different inorganic aerosol, was retrieved using a Bessel beam optical trap. Nevertheless, although the optical trapping is suitable and powerfully established for the scattering of spherical aerosol, instabilities arise for irregular shapes and for materials that absorb radiation in the wavelength used for trapping. Therefore, alternative tools must be developed to confine different specimens, allowing their robust assessment and the improvement of physicochemical models.

The electrodynamic balance, also called Paul trap (PT), provides benefits as an alternative to optical trapping because it is able to trap a wider range of materials. Although, as mentioned above, its use has been largely limited to larger particles due to the accuracy ($\pm$ 0.25 µm) on the geometrical optics approximation to estimate particle size [24], they are very well suited to the levitation of particles in the fine mode. Conveniently coupled with optical systems with high numerical aperture (NA), it is feasible to achieve sensitivity and control similar to what is obtained with optical tweezers [29–31]. Indeed, Bullier et al. [32]. reported that the PT setup enabled to reach signal-to-noise ratios as good as 10^6 with a displacement sensitivity better than 10^{-16} m^2/Hz. Further, Bullier et al. [33] found that the charge on the nanoscillator is stable over timescale of at least two weeks and they can estimate the mass of the oscillator with a 3% uncertainty using a linear Paul trap. Therefore, this approach represents an alternative and improvement tool to standard optical traps.

In this work, we demonstrate that a conveniently designed Paul trap can be used to examine the physicochemical properties of aerosols in the fine mode regime during evaporation. Although semi-volatile organic 1,2,6-hexanetriol and glycerol compounds are not atmospheric aerosol relevant, we use them as a good benchmark model to estimate the validity of the PT approach for studying droplet volatilities in low relative humidity (RH<10%). This arrangement allows us to perceive small size changes easily without perturbing the trapping stability. Measurements of gas-droplet partitioning of semi-volatile components have been reported.
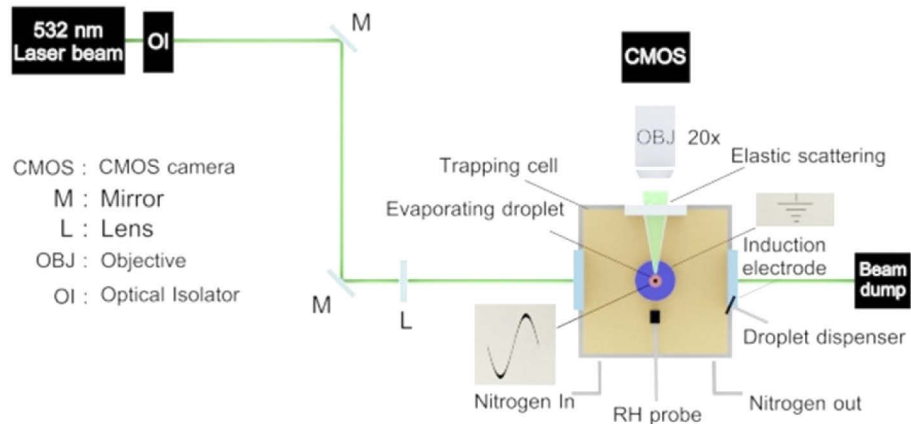
2. Experimental setup

2.1. Electrodynamic Paul trap: levitation of droplets

A schematic diagram of the PT and an artistic representation of the trapping scheme are shown in Figs. 1(a) and 1(b), respectively.

The PT is located inside a custom-made chamber and operated at atmospheric pressure and room temperature, with all measurements performed between 295 and 300 K (Fig. 2).

This platform is formed by two conical electrodes separated by 1.5 mm that are enclosed by grounded cylindrical shields which has a diameter of 2 cm and 3 cm of length. An AC voltage signal $V_0 \cos(\omega_d t)$ is applied to the cones; the typical applied amplitude V_0 is of 2 kV at a
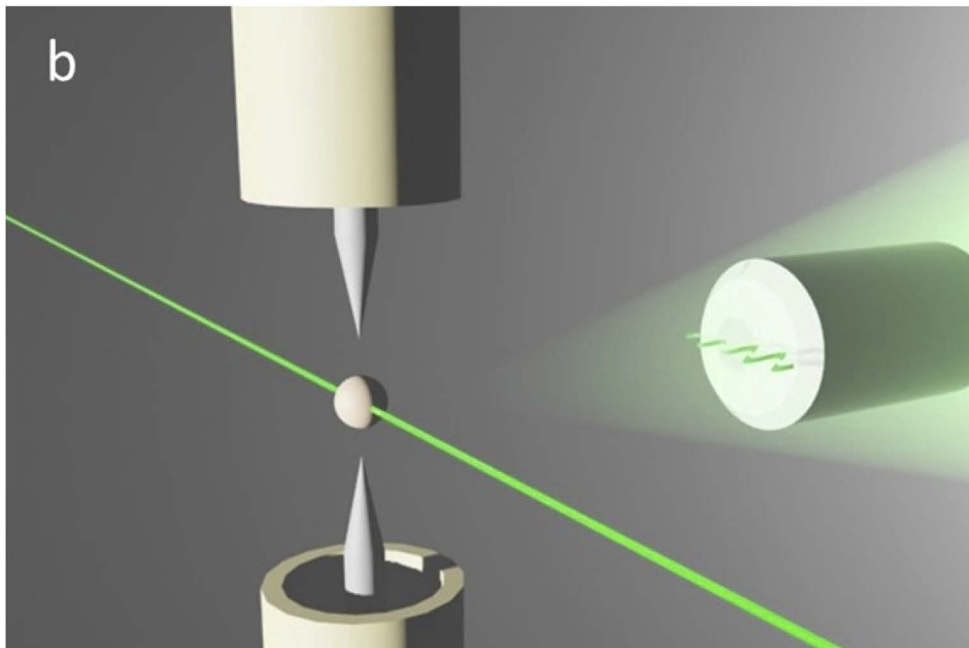
Fig. 1. a) The schematic setup of the Paul trap experiment, b) artistic representation of the trapping scheme.
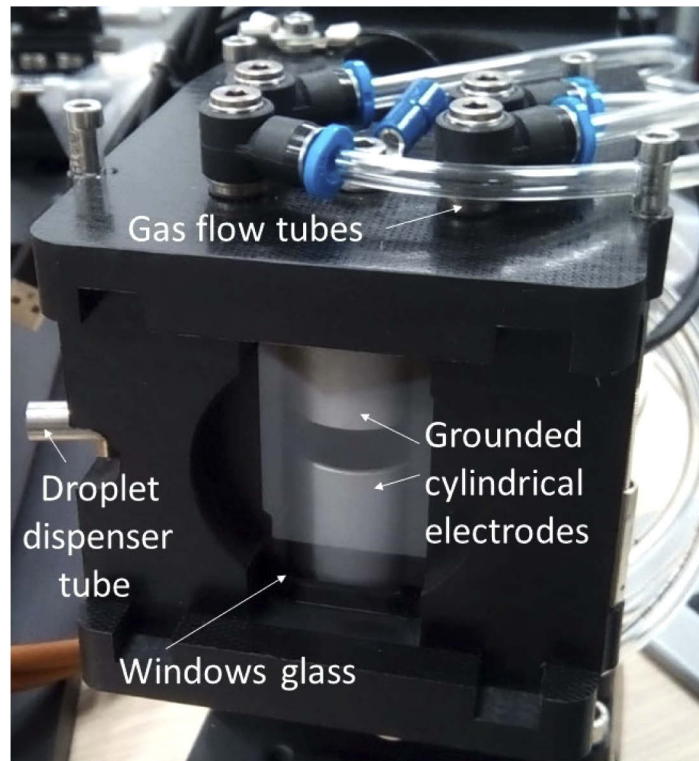
Fig. 2. Picture of the custom-made chamber, where the grounded cylinders are clearly seen housed.

frequency $\omega_d = 2\pi \ x \ 2000 Hz$. With these parameters, the PT was capable of trapping droplets ranging between 500 nm up to few microns in radius. The design principles of this technique have been reported elsewhere [29,34]. Droplets are injected into the PT by applying a square voltage pulse (or sequence of pulses) to a droplet-on-demand micro-dispenser (Microfab MJ-ABP-01). Droplets of opposite polarity to the voltage applied to an induction electrode (with a voltage ranging from 50 to 600 V), placed between the droplet dispenser and the trap, are attracted and injected into the PT. The RH inside the trapping cell was monitored using a capacitance probe (Honeywell). The RH is controlled using dry nitrogen, introduced from the top of the chamber at flow rates up to 20 cm^3/min, low enough to ensure that RH falls below 10%. The aerodynamic force on the droplet is small, and therefore does not significantly affect droplet position, as we discuss below.

An aperture at the side of the trapping cell gives access to a horizontally propagating Gaussian laser beam of $\lambda = 532$ nm which illuminates the droplet for angularly resolved elastic scattering measurements of the droplet size. A CMOS camera (Thorlabs, DCC1546M) coupled to a 20× long working distance objective (Mitutoyo) with a numerical aperture (NA) of 0.42, orientated 90° to the laser beam, is used to capture the phase function (PF) from a single trapped droplet. Figure 3 shows example the PF image of a 1,2,6-hexanetriol droplet illuminated with laser of $\lambda = 532$ nm in RH below 10%. The angular scattering lobe structure predicted by Mie theory is clearly observed.

Dry nitrogen is injected into the trapping cell until the in-cell RH probe reports a stable value below 10%. Initially many droplets are dispensed into the trapping cell and the RH increases rapidly up to 15–25%. An abrupt increase on the drive frequency of the PT together with gas
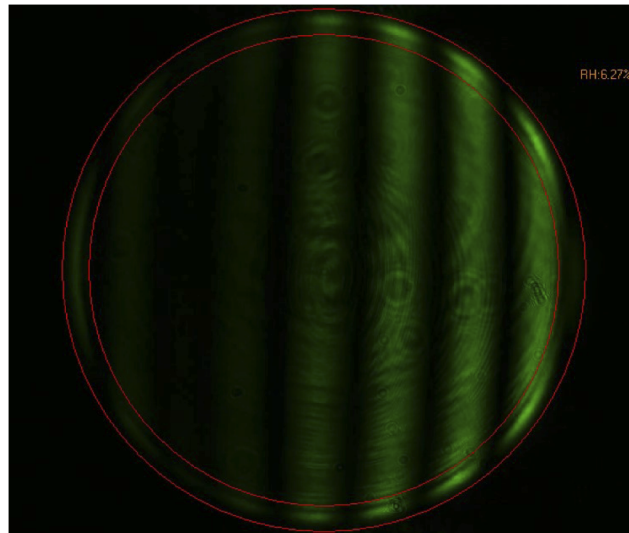
Fig. 3. PF image of a trapped 1,2,6-hexanetriol droplet.

flow is used to purge the cell of excess aerosol. Finally, a single droplet is kept in RH below 10% after a few minutes. When a steady equilibrium is reached, the droplet is levitated in the middle of the two tips of the cones.

3. Results

For benchmarking the new setup and assessing its validity, it is common to determine the radius of a spherical droplet of constant composition during the evaporation process and determine whether the data can be reproduced using Mie theory. 1,2,6-hexanetriol and glycerol are semi-volatile organic compounds that are relatively non-hygroscopic. Although they are not atmospheric relevant, have been chosen as ideal systems to validate that type of configuration in numerous studies [16,20,21]. Potential uncertainty sources in our experiment will be non-zero RH, the noise in the PFs associated to an unappropriated selection of the scattering angular range in the simulations and the impurity traces in semi-volatile organic levitated droplets.

The radius r of the trapped droplet is determined from the best fit to the experimental PF from a simulated library of PFs obtained from Mie theory across a realistic range of radii, considering a real refractive index (n) at $\lambda = 532$ nm. The Pearson correlation coefficient, c, between each of the simulated and measured PFs is calculated. For each measured PF, the simulation with the highest correlation defines the best-fit radius of the droplet for the corresponding value of n. This process is evaluated for the entire data set and the mean arithmetic correlation value $\bar{c}$ is calculated for all of them. It is possible identify the best-fit n at $\lambda = 532$ nm which maximizes $\bar{c}$ out of this data set. This correlation procedure has been traditionally employed by other authors [16,20,28,35].

Eleven different 1,2,6-hexanetriol droplets were electrodynamically trapped and their elastic scattering recorded as they evaporate over time. For these droplets, the experimentally acquired signal of the scattering intensity versus scattering angle was compared with simulations to retrieve the size and refractive index of the droplet. An example of the agreement between theory and experiment is shown in Fig. 4 for a droplet of 2394 nm of radius, where prominent peaks, valleys and shapes are remarkably similar in both curves.

The fitting procedure is as follows. At every time frame, the out-of-focus image (see Fig. 3) is converted into the PF (Fig. 4), and the best values for n and r are obtained from comparison
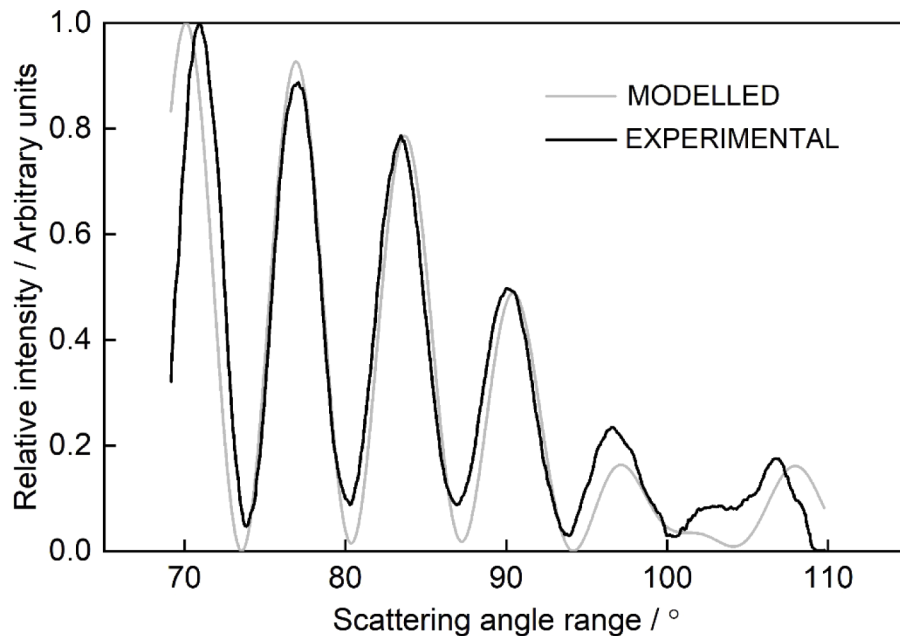
Fig. 4. Modelled and experimental phase function versus scattering angle range for a levitated 1,2,6-hexanetriol droplet of 2394 nm of radius.

with Mie theory. Then, we compute the mean value of the refractive index determined from all the measurements (the eleven droplets at all times), obtaining $n = 1.484 \pm 0.002$, where error accounts for one standard deviation. This error in n causes an uncertainty on the estimation of droplet radius, as we illustrate in Fig. 5. In order to estimate it, we fit again every PF to obtain r for all the droplets with the mean n, as well as $n \pm 0.002$, providing an uncertainty interval for every r. Figure 5(a) shows the obtained radii for the mean n as well as its uncertainty (1.484 ± 0.002) for one particular droplet of 1500 nm of radius when it is trapped. The top inset is a zoom for a specific radius range where it is appreciable the difference in radii for the different n. The bottom inset shows the correlation coefficient ($\bar{c}$) versus n during fitted procedure for entire PFs data set between experimental and modelled PFs. Overall, the accuracy reported here in radius is acceptable, estimated within 10 nm of the correct size if the n is known typically within the error range due the uncertainty in the RH (±0.02) [36].

We also quantified the stability of the droplet position from the image obtained with the CMOS camera [Fig. 5(b)]. Excursions of the droplet smaller than 15 μm from the mean position along the direction of propagation of the laser beam (y) are observed. Notice that this is the axis where the largest fluctuations are expected, since the nitrogen flux is directed along this axis, and the electric field, and hence the confinement, are weaker in out PT design [30]. Different features can be seen in Fig. 5(b). First, the sharp peaks arise when the droplet size is such that there is a scattering resonance with the laser light, leading to stronger radiation pressure that pushes the droplet along the direction of propagation of the beam. This is clearly seen from the fact that that these kicks are always in the positive direction, along the propagation direction of the beam. A second feature observed in Fig. 5(b) is the presence of slower drifts of the position of the droplet. We attribute these to motion due to the gas flow in the chamber.

Finally, we also observe a noisy component that is due to Brownian motion of the droplet in the trap. In this case, we quantified the standard deviation from the curve without considering the peaks due to resonances neither the drifts due to gas flow, which is found to be smaller than
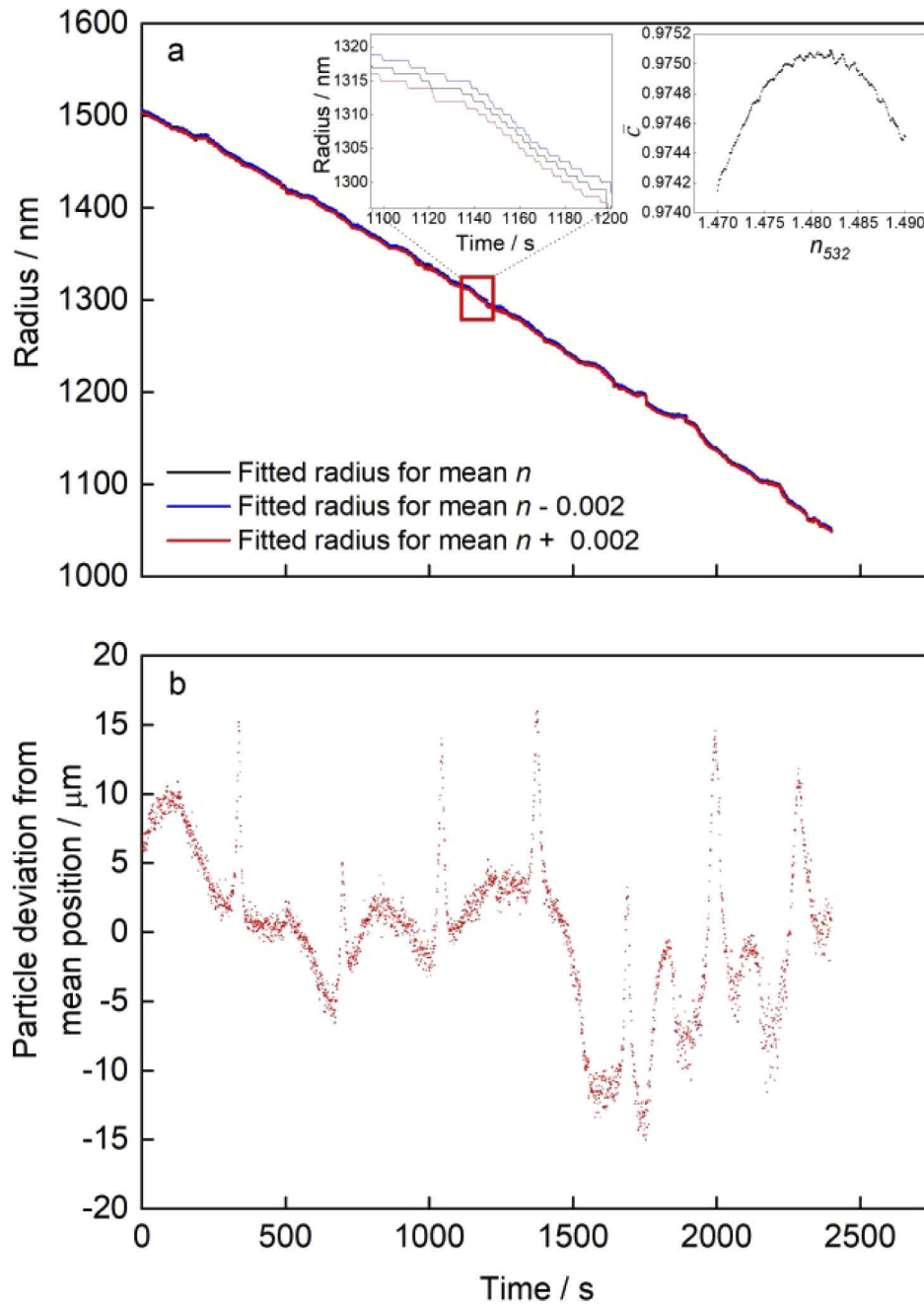
Fig. 5. a) The fitted radius versus time for one 1,2,6-hexanetriol droplet for the estimated mean value of *n* and for its uncertainty (±0.002). The top inset is a zoom for a specific radius range. The bottom inset shows the mean correlation coefficient $\bar{c}$ between the measured and simulated PFs as a function of *n* for the radius data of one 1,2,6-hexanetriol droplet. (b) Particle position variation over the course of the measurement.

1 µm, in agreement with theoretical predictions [30]. Deviations on the droplet position higher than 200 µm were found in Ref. [20] using a Bessel beam optical trap and glycerol as compound. Recently, Bullier et al. [32] reported a displacement of up to 40 µm for confined nanoparticles in a linear Paul trap. Therefore, the stability of the droplet position is excellent in our experiment and the determination of the droplet size from PFs is not compromised by large excursions of the droplet.

The evolving sizes estimated for eleven 1,2,6-hexanetriol droplets obtained from the PFs are shown in Fig. 6(a). We see that the variability in both the initial and final size is significant. The largest droplet is initially trapped at a radius of 2157 nm, and the smallest droplet evaporates to a radius of 493 nm. The variability is likely due to the stochastic nature of the charging process. In our protocol, we leave the droplet escape out of the trap when the PF starts to blur in the image. The blurring is likely due to an increase in both the Brownian fluctuations and the micromotion as the charge to mass ratio decreases in the case of the smaller droplets, [29]. In any case, this plot illustrates the high level of reproducibility that can be achieved between slopes of the time dependence of the radius of the evaporating semi-volatile organic aerosol.

The relationship of the single-component droplet evaporation rate with respect to the droplet surface area or radius squared over time is given by the Maxwell's equation [10]:

$$\frac{dr^2}{dt} = \frac{2D_{ij}M_i}{R\rho}\left(\frac{p_\infty}{T_\infty} - \frac{p}{T}\right), \tag{1}$$

where D_{ij} is the gas phase diffusion constant of i-th specie in the surrounding medium j estimated using the Chapman-Enskog method [37]. In Eq. (1), M_i is the molecular weight, ρ the density of the droplet, R the gas constant, p and p_∞ are the partial pressures of the species at the surface of the droplet and at infinite distance, respectively, and T and T_∞ the corresponding temperatures. Additionally, at droplet sizes below 1 µm in diameter other adjustments such as surface curvature (Kelvin effect) and atmospheric molecular mean-free-path considerations are also required [38]. Taking into account the vapour pressure of the component i at infinite distance is negligible, Eq. (1) can be reduced to:

$$\frac{dr^2}{dt} = \frac{2D_{ij}pM_i}{RT\rho m_i} \tag{2}$$

where m_i is the mass fraction of solute i. No other component in the surrounding gas will combine or react with the droplet. Therefore, the pure component vapour pressure, p_0, is related to the determined vapour pressure by $p = p_0\gamma_i x_i$, where γ_i is the activity coefficient and x_i is the mole fraction of species i in the droplet. In this experiment we assume that both activity coefficient and the mole fraction are equal to unity. If the surrounding gas is moving with respect to the droplet, as in our setup, then the evaporation rate will also depend on the gas-flow rate and hence, the velocity (Sherwood number) [39]. For the experimental conditions in the present work, the maximum value of the Sherwood number has been estimated to be in the range 2.03-2.07, remaining almost constant during the entire period of an experiment. Temperature control has not been implemented yet.

Figure 6(b) shows the radius-squared changes observed for the eleven 1,2,6-hexanetriol droplets radius plotted in Fig. 6(a) as they evaporate over time. The slopes of the lineal fits reveal evaporation rates spanning from 4.05×10^{-16} to 5.62×10^{-16} m^2/s, where in the worst case the correlation coefficient is 0.996. The quality of our result is a consequence of the stability of our trap and the efficiency in collecting the elastic scattering. Figure 6(c) summarises the results of the eleven pure component vapour pressures (black dots) calculated from the analysis above. This plot includes mean value (black line) with one standard deviation (shaded area). From the evaporation rate, the mean vapour pressure estimated for all eleven droplets is of $(4.0 \pm 0.4) \times 10^{-4}$ Pa, with values ranging from $(3.3 \pm 0.3) \times 10^{-4}$ to $(4.6 \pm 0.3) \times 10^{-4}$ Pa. Overall, the
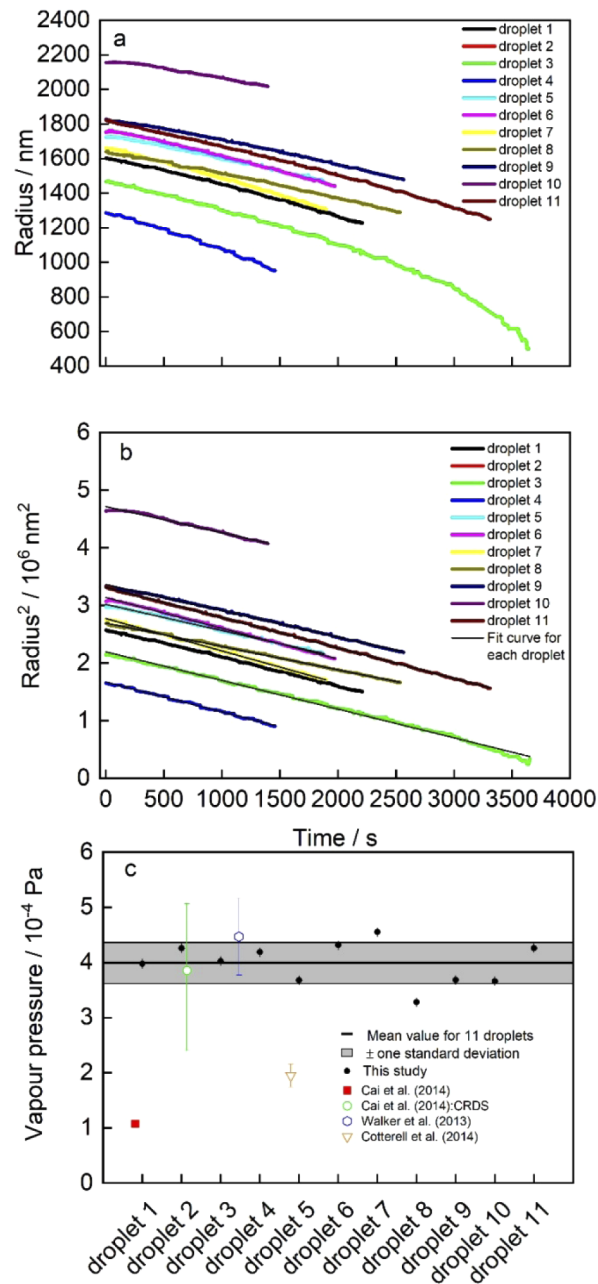
Fig. 6. a) Change in measured radius over time for eleven 1,2,6-hexanetriol droplets, b) the radius-squared as a function of time for the eleven evaporating droplets. The black lines correspond to the lineal fit, c) vapour pressures from eleven droplets (black dots) where the mean value is indicated by the black line and one standard deviation by the shaded area. Error bars are added to each individual vapour pressure value. References values of vapour pressure are included.

estimated vapour pressures fall within the value ranges obtained in previous publications [see Fig. 6(c)], apart from [11] and [16] for which the reported data are lower.
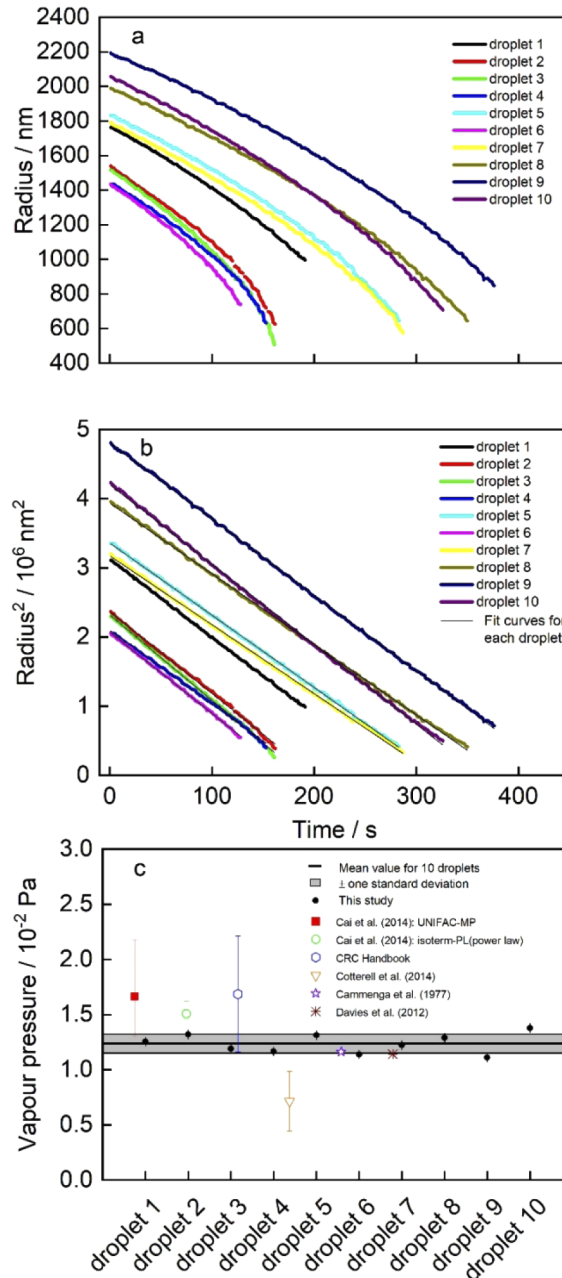

Fig. 7. a) Change in measured radius over time for ten glycerol droplets, b) the radius-squared as a function of time for the ten evaporating droplets. The black lines correspond to the lineal fit, c) vapour pressures from ten droplets (black dots) where the mean value is indicated by the black line and one standard deviation by the shaded area. Error bars are added to each individual vapour pressure value. Reference values of vapour pressure are included.

Compared to 1,2,6-hexanetriol, glycerol droplets evaporate faster owing to the much higher vapour pressure. The evaporation profile recorded from ten glycerol droplets is again highly reproducible under a fixed set of conditions [see Fig. 7(a)]. Figure 7(b) shows the radius squared of the data shown in Fig. 7(a). The slopes of the fitting reveal evaporation rates ranging from 1.01×10^{-14} to 1.23×10^{-14} m^2/s, giving values of vapour pressures from $(0.0117 \pm 0.0012) \times 10^{-2}$ to $(0.0138 \pm 0.0031) \times 10^{-2}$ Pa with a mean value of $(1.24 \pm 0.08) \times 10^{-2}$ Pa. These values are in agreement with previous results published in [40] (0.0118 Pa) and [24] (0.0116 Pa). In spite of the higher volatility of this compound compared to 1,2,6-hexanetriol, the precision of our measurements is demonstrated by the high degree of the lineal fit achieved with correlation coefficient values in the range [0.998-0.999]. Figure 7(c) summarizes the results from the ten pure glycerol droplets for the estimation of the vapour pressures (black dots), their mean value (black line) and the one standard deviation (shaded area). The level of reproducibility of the vapour pressure for ten droplets is quite reasonable when we compare with the variability showed from other studies whose references are included in this plot for comparison.

4. Conclusion

In this work, a PT is used to demonstrate a new approach to measure the droplet size in the fine mode range during evaporation. We validated our platform using two semi-volatile organic aerosols: 1,2,6-hexanetriol and glycerol. To our knowledge, this is the first report using a PT to study the evaporation of single liquid droplets in the fine mode. Experimental phase functions are fitted to Mie theory to accurately determine droplet radii capable of revealing changes in size as small as 10 nm. The evaporation rates retrieved from radius-squared versus time present a high precision level, which we attribute to the increased stability of the droplets in this platform. The capability of this PT to access the vapour pressure of semi-volatile organic aerosols is successfully demonstrated with an acceptable reproducibility, quantified by the low standard deviation.

Overall, this platform is an accurate and highly useful tool allowing precise determination of changes in size with minimal computation time. The PT has the potential for a complete characterization of physicochemical aerosol properties. Finally, the ability to confine any type of droplet could be used to explore complex droplet shapes including light absorbent materials.

Disclosures

The authors declare that there are no conflicts of interest related to this article.

References

1. T. F. Stocker, D. Qin, G.-K. Plattner, M. Tignor, S. K. Allen, J. Boschung, A. Nauels, Y. Xia, V. Bex, and P. M. Midgley, "Climate change 2013: The physical science basis," *Contrib. Work. Gr. I to fifth Assess. Rep. Intergov. panel Clim. Chang.* 1535, (2013).
2. J. A. Bernstein, "Alexis N, Barnes C, Bernstein IL, Bernstein JA, Nel A, Peden D, Diaz-Sanchez D, Tarlo SM, and Williams PB," J. Allergy Clin. Immunol. **114**(5), 1116–1123 (2004).

3. R. Hołyst, M. Litniewski, D. Jakubczyk, K. Kolwas, M. Kolwas, K. Kowalski, S. Migacz, S. Palesa, and M. Zientara, "Evaporation of freely suspended single droplets: experimental, theoretical and computational simulations," Rep. Prog. Phys. **76**(3), 034601 (2013).

4. U. Pöschl, "Atmospheric aerosols: composition, transformation, climate and health effects," Angew. Chem., Int. Ed. **44**(46), 7520–7540 (2005).

5. J. H. Seinfeld and S. N. Pandis, "From air pollution to climate change," Atmos. Chem. Phys. **1326**, 1152 (1998).

6. T. D. Wheeler and A. D. Stroock, "The transpiration of water at negative pressures in a synthetic tree," Nature **455**(7210), 208–212 (2008).

7. N. G. Khlebtsov and L. A. Dykman, "Optical properties and biomedical applications of plasmonic nanoparticles," J. Quant. Spectrosc. Radiat. Transfer **111**(1), 1–35 (2010).

8. M. B. Dolovich and R. Dhand, "Aerosol drug delivery: developments in device design and clinical use," Lancet **377**(9770), 1032–1045 (2011).

9. A. E. Haddrell, D. Lewis, T. Church, R. Vehring, D. Murnane, and J. P. Reid, "Pulmonary aerosol delivery and the importance of growth dynamics," Ther. Delivery **8**(12), 1051–1061 (2017).

10. U. K. Krieger, C. Marcolli, and J. P. Reid, "Exploring the complexity of aerosol particle properties and processes using single particle techniques," Chem. Soc. Rev. **41**(19), 6631–6662 (2012).

11. C. Cai, D. J. Stewart, J. P. Reid, Y. Zhang, P. Ohm, C. S. Dutcher, and S. L. Clegg, "Organic component vapor pressures and hygroscopicities of aqueous aerosol measured by optical tweezers," J. Phys. Chem. A **119**(4), 704–718 (2015).

12. E. Dinar, A. A. Riziq, C. Spindler, C. Erlick, G. Kiss, and Y. Rudich, "The complex refractive index of atmospheric and model humic-like substances (HULIS) retrieved by a cavity ring down aerosol spectrometer (CRD-AS)," Faraday Discuss. **137**, 279–295 (2008).

13. J. Michel Flores, R. Z. Bar-Or, N. Bluvshtein, A. Abo-Riziq, A. Kostinski, S. Borrmann, I. Koren, and Y. Rudich, "Absorbing aerosols at high relative humidity: linking hygroscopic growth to optical properties," Atmos. Chem. Phys. **12**(12), 5511–5521 (2012).

14. R. E. H. Miles, A. E. Carruthers, and J. P. Reid, "Novel optical techniques for measurements of light extinction, scattering and absorption by single aerosol particles," Laser Photonics Rev. **5**(4), 534–552 (2011).

15. C. Braun and U. K. Krieger, "Two-dimensional angular light-scattering in aqueous NaCl single aerosol particles during deliquescence and efflorescence," Opt. Express **8**(6), 314–321 (2001).

16. M. I. Cotterell, B. J. Mason, A. E. Carruthers, J. S. Walker, A. J. Orr-Ewing, and J. P. Reid, "Measurements of the evaporation and hygroscopic response of single fine-mode aerosol particles using a Bessel beam optical trap," Phys. Chem. Chem. Phys. **16**(5), 2118–2128 (2014).

17. J. F. Davies, "Mass, charge, and radius of droplets in a linear quadrupole electrodynamic balance," Aerosol Sci. Technol. **53**(3), 309–320 (2019).

18. F. K. A. Gregson, J. F. Robinson, R. E. H. Miles, C. P. Royall, and J. P. Reid, "Drying Kinetics of Salt Solution Droplets: Water Evaporation Rates and Crystallization," J. Phys. Chem. B **123**(1), 266–276 (2019).

19. M. B. Hart, V. Sivaprakasam, J. D. Eversole, L. J. Johnson, and J. Czege, "Optical measurements from single levitated particles using a linear electrodynamic quadrupole trap," Appl. Opt. **54**(31), F174 (2015).

20. B. J. Mason, M. I. Cotterell, T. C. Preston, A. J. Orr-Ewing, and J. P. Reid, "Direct measurements of the optical cross sections and refractive indices of individual volatile and hygroscopic aerosol particles," J. Phys. Chem. A **119**(22), 5701–5713 (2015).

21. J. S. Walker, A. E. Carruthers, A. J. Orr-Ewing, and J. P. Reid, "Measurements of light extinction by single aerosol particles," J. Phys. Chem. Lett. **4**(10), 1748–1752 (2013).

22. A. A. Zardini, U. K. Krieger, and C. Marcolli, "White light Mie resonance spectroscopy used to measure very low vapor pressures of substances in aqueous solution aerosol particles," Opt. Express **14**(15), 6951–6962 (2006).

23. A. J. Huisman, U. Krieger, A. Zuend, C. Marcolli, and T. Peter, "Vapor pressures of substituted polycarboxylic acids are much lower than previously reported," Atmos. Chem. Phys. **13**(13), 6647–6662 (2013).

24. J. F. Davies, A. E. Haddrell, and J. P. Reid, "Time-resolved measurements of the evaporation of volatile components from single aerosol droplets," Aerosol Sci. Technol. **46**(6), 666–677 (2012).

25. J. F. Davies, A. E. Haddrell, A. M. J. Rickards, and J. P. Reid, "Simultaneous analysis of the equilibrium hygroscopicity and water transport kinetics of liquid aerosol," Anal. Chem. **85**(12), 5819–5826 (2013).

26. J. Wang, D. J. Jacob, and S. T. Martin, "Sensitivity of sulfate direct climate forcing to the hysteresis of particle phase transitions," J. Geophys. Res. **113**(D11), D11206 (2008).

27. C. L. Heald, D. A. Ridley, J. H. Kroll, S. R. H. Barrett, K. E. Cady-Pereira, M. J. Alvarado, and C. D. Holmes, "Contrasting the direct radiative effect and direct radiative forcing of aerosols," (2014).

28. M. I. Cotterell, R. E. Willoughby, B. R. Bzdek, A. J. Orr-Ewing, and J. P. Reid, "A complete parameterisation of the relative humidity and wavelength dependence of the refractive index of hygroscopic inorganic aerosol particles," Atmos. Chem. Phys. **17**(16), 9837–9851 (2017).

29. G. P. Conangla, A. W. Schell, R. A. Rica, and R. Quidant, "Motion control and optical interrogation of a levitating single nitrogen vacancy in vacuum," Nano Lett. **18**(6), 3956–3961 (2018).

30. G. P. Conangla, R. A. Alarcón, and R. Quidant, "Extending vacuum trapping to absorbing objects with hybrid Paul-optical traps," arXiv Prepr. arXiv2005.05486 (2020).

31. D. S. Bykov, P. Mestres, L. Dania, L. Schmöger, and T. E. Northup, "Direct loading of nanoparticles under high vacuum into a Paul trap for levitodynamical experiments," Appl. Phys. Lett. **115**(3), 034101 (2019).
32. N. P. Bullier, A. Pontin, and P. F. Barker, "Super-resolution imaging of a low frequency levitated oscillator," Rev. Sci. Instrum. **90**(9), 093201 (2019).
33. N. P. Bullier, A. Pontin, and P. F. Barker, "Characterisation of a charged particle levitated nano-oscillator," J. Phys. D: Appl. Phys. **53**(17), 175302 (2020).
34. G. P. Conangla, D. Nwaigwe, J. Wehr, and R. A. Rica, "Overdamped dynamics of a Brownian particle levitated in a Paul trap," Phys. Rev. A **101**(5), 053823 (2020).
35. A. Bain, A. Rafferty, and T. C. Preston, "Determining the size and refractive index of single aerosol particles using angular light scattering and Mie resonances," J. Quant. Spectrosc. Radiat. Transfer **221**, 61–70 (2018).
36. C. Cai, A. Marsh, Y. Zhang, and J. P. Reid, "Group contribution approach to predict the refractive index of pure organic components in ambient organic aerosol," Environ. Sci. Technol. **51**(17), 9683–9690 (2017).
37. S. Chapman, T. G. Cowling, and D. Burnett, *The Mathematical Theory of Non-Uniform Gases: An Account of the Kinetic Theory of Viscosity, Thermal Conduction and Diffusion in Gases* (Cambridge University, 1990).
38. J. F. Davies, A. Zuend, and K. R. Wilson, "The role of evolving surface tension in the formation of cloud droplets," Atmos. Chem. Phys. **19**(5), 2933–2946 (2019).
39. A. K. Ray, R. D. Johnson, and A. Souyri, "Dynamic behavior of single glycerol droplets in humid air streams," Langmuir **5**(1), 133–140 (1989).
40. H. K. Cammenga, F. W. Schulze, and W. Theuerl, "Vapor pressure and evaporation coefficient of glycerol," J. Chem. Eng. Data **22**(2), 131–134 (1977).